Journal of Materials Science and Chemical Engineering, 2026, 14(4), 53-74
https://www.scirp.org/journal/msce
ISSN Online: 2327-6053
ISSN Print: 2327-6045

Numerical Investigation and Optimization of a CdTe/Perovskite ($CH_3NH_3SnI_3$) Heterojunction Solar Cell Using SCAPS-1D

Souleymane Tuo[1], Boris IRIE-Bi[1*], Sampson Oyedele[2], Kalou F. Bimun[1], Yapi A. Simon[3], Aka Boko[2]

[1]Department of Physics and Department of Chemistry, Faculty of Science and Technology, University of Man (U-Man), Man, Côte d'Ivoire
[2]Department of Mathematics, Physics and Informatic, University of Nangui Abrogoua (UNA), Abidjan, Côte d'Ivoire
[3]Laboratory of Technonolgies (Lab-Tech), University Felix Houphouët Boingy, Abidjan, Côte d'Ivoire
Email: *lezie.irie-bi@univ-man.edu.ci

How to cite this paper: Tuo, S., IRIE-Bi, B., Oyedele, S., Bimun, K.F., Simon, Y.A. and Boko, A. (2026) Numerical Investigation and Optimization of a CdTe/Perovskite ($CH_3NH_3SnI_3$) Heterojunction Solar Cell Using SCAPS-1D. *Journal of Materials Science and Chemical Engineering*, **14**, 53-74.
https://doi.org/10.4236/msce.2026.144004

Received: February 2, 2026
Accepted: April 26, 2026
Published: April 29, 2026

Abstract

Identifying efficient and environmentally sustainable alternatives to silicon remains a major challenge for next-generation photovoltaics. Here, a CdS/CdTe/$CH_3NH_3SnI_3$/Spiro-OMeTAD dual-absorber heterojunction solar cell is investigated using the SCAPS-1D simulation framework, where CdTe and the lead-free tin-based perovskite $CH_3NH_3SnI_3$ jointly form the active absorbing layers. A systematic parametric study is performed to evaluate the influence of absorber thickness, doping concentration and operating temperature on device performance. The simulations show that a favorable band alignment at the CdTe/$CH_3NH_3SnI_3$ interface, together with balanced absorber thicknesses and moderate doping, enhances charge separation and reduces recombination losses. Under optimized and intentionally idealized numerical assumptions, the proposed device reaches an open-circuit voltage of 1.017 V, a short-circuit current density of 34.429 mA cm^{-2}, a fill factor of 82.07%, and a theoretical power conversion efficiency of 28.73%. The observed trends clearly highlight the potential of combining CdTe with lead-free tin-based perovskites in a dual-absorber heterojunction architecture. This study provides valuable design guidelines for the development of high-efficiency, lead-free thin-film solar cells and offers a solid theoretical framework for future experimental investigations.

Keywords

CdTe/Perovskite Heterojunction, Lead-Free Perovskite Solar Cell,

SCAPS-1D Simulation, Dual Absorber Solar Cell, Photovoltaic Optimization, Thin-Film Photovoltaics

1. Introduction

The ongoing global transition toward low-carbon energy systems continues to drive sustained research efforts in photovoltaic technologies. Although crystalline silicon solar cells dominate the current market due to their technological maturity and long-term reliability, their efficiency is fundamentally constrained by the Shockley-Queisser detailed-balance limit for single-junction devices [1]. Under standard illumination conditions, this theoretical ceiling lies in the range of approximately 30% - 33%, depending on the bandgap and recombination assumptions [2]. As a result, improving spectral utilization and charge-carrier management within structurally simple device configurations remains an important scientific objective.

Among thin-film technologies, CdTe has established itself as a robust and industrially viable absorber material. Its near-optimal bandgap, high absorption coefficient, and favorable transport properties have enabled competitive efficiencies with scalable fabrication processes. However, further performance improvements are increasingly limited by recombination losses and incomplete use of the solar spectrum [3] [4].

In parallel, halide perovskites have attracted considerable attention owing to their strong optical absorption and promising charge-transport characteristics. While lead-based perovskites have demonstrated remarkable efficiencies, environmental and toxicity concerns associated with Pb have motivated the exploration of lead-free alternatives [5]. Tin-based perovskites, such as $CH_3NH_3SnI_3$, exhibit a suitable bandgap and strong visible-light absorption, but their performance is constrained by intrinsic challenges including Sn^{2+} oxidation, defect-mediated recombination, and stability issues. These limitations reduce both efficiency and long-term operational reliability [6] [7].

Combining complementary absorber materials within a dual-absorber heterojunction architecture represents a conceptually simple strategy to address these limitations. Unlike multi-terminal tandem structures, dual-absorber heterojunctions maintain fabrication simplicity while enabling extended spectral absorption and modified internal electric-field distributions [8]. In this context, integrating CdTe with $CH_3NH_3SnI_3$ is of particular interest. CdTe contributes established electronic stability and near-infrared absorption, whereas $CH_3NH_3SnI_3$ enhances visible-light absorption and offers compatible band alignment. Despite the individual maturity of CdTe-based devices and the extensive numerical studies of $CH_3NH_3SnI_3$ single-absorber solar cells, the coupled electrostatic behavior and recombination dynamics of CdTe/$CH_3NH_3SnI_3$ dual-absorber heterojunctions have not been systematically examined.

Numerical simulation provides a controlled framework for investigating such coupled effects prior to experimental implementation. The SCAPS-1D platform, based on the self-consistent solution of Poisson's equation and carrier continuity equations within the drift-diffusion formalism, allows systematic evaluation of absorber thickness, doping concentration, defect density, and interfacial band alignment. Nevertheless, simulated performance remains dependent on modeling assumptions regarding material quality and interface ideality, and must therefore be interpreted within clearly defined theoretical boundaries [9].

In this study, we present a systematic SCAPS-1D analysis of a CdS/CdTe/$CH_3NH_3SnI_3$/Spiro-OMeTAD dual-absorber heterojunction solar cell. By conducting controlled parametric investigations, we aim to clarify the physical mechanisms governing charge separation and recombination in this hybrid configuration and to establish realistic design trends under well-defined numerical assumptions. The objective is not to claim experimentally attainable record efficiencies, but rather to provide a physically consistent theoretical framework that may inform future experimental efforts toward efficient and environmentally sustainable thin-film photovoltaic devices.

2. Methodology

2.1. Device Configuration

Figure 1 presents the schematic structure (Figure 1(a)) and the corresponding energy-band diagram (Figure 1(b)) of the proposed solar cell. The device consists of a CdS/CdTe/$CH_3NH_3SnI_3$/Spiro-OMeTAD multilayer stack configured as an inverted n-p heterojunction. In the simulated structure, CdTe is defined as an n-type absorber layer, while $CH_3NH_3SnI_3$ is treated as a p-type absorber, forming the primary depletion region at their interface. This junction is responsible for the main built-in electric field governing charge separation and carrier transport within the device.

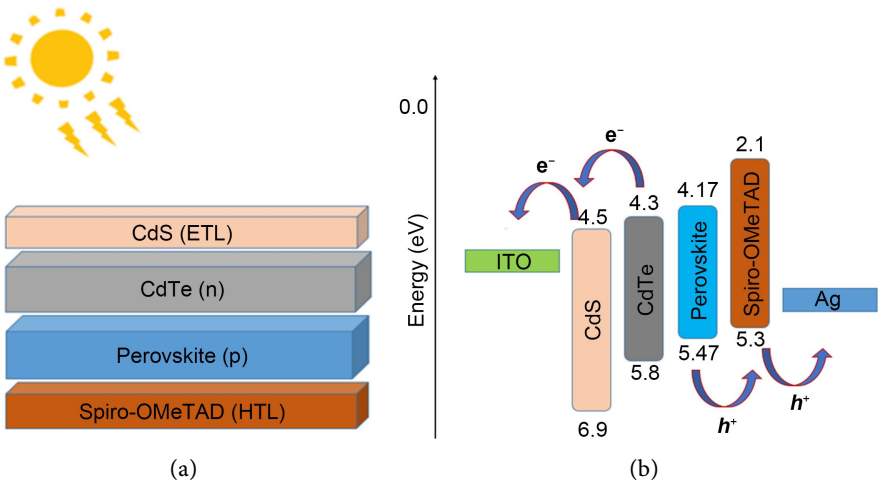

(a) (b)

Figure 1. Structure of the solar cell: (a) Planar heterojunction configuration, (b) Energy diagram.

CdS acts as the electron transport layer (ETL), facilitating electron extraction toward the front contact while blocking holes, whereas Spiro-OMeTAD serves as the hole transport layer (HTL), promoting hole collection and suppressing electron back-injection [10]. The selection of this inverted n-p configuration allows controlled modulation of band alignment and internal electric-field distribution at the CdTe/$CH_3NH_3SnI_3$ interface within the SCAPS framework.

ITO and Ag are employed as the front and rear contacts, respectively. In the simulations, their work functions are explicitly defined, and ohmic boundary conditions are assumed to ensure selective carrier extraction without introducing additional Schottky barriers. Surface recombination velocities at the contacts are also specified in accordance with the simulation settings described below.

The device architecture is modeled assuming abrupt and electronically well-defined interfaces. Fixed interface defect densities are introduced between adjacent layers; however, a detailed sensitivity analysis of interfacial recombination is beyond the scope of the present study. It should therefore be emphasized that the simulated behavior reflects idealized junction conditions and defines a theoretical performance envelope rather than a fully realistic experimental scenario.

2.2. Material Parameters Used in Simulation

The material parameters used in the SCAPS-1D simulations are summarized in **Table 1**, including bandgap energy, electron affinity, relative permittivity, effective density of states, carrier mobilities, and baseline doping concentrations for each layer. The baseline values are taken from previously published experimental and numerical reports to ensure comparability with the literature and to provide a consistent starting point for the parametric studies performed in this work [11] [12].

In order to investigate the electrostatic limits of charge separation and recombination control in the CdTe/$CH_3NH_3SnI_3$ heterojunction, the doping concentrations of selected layers particularly the CdTe and $CH_3NH_3SnI_3$ absorbers, were deliberately varied over a wide numerical range (1×10^{11} - 1×10^{22} cm^{-3}). We emphasize that the upper end of this range is not intended to represent experimentally attainable doping in real materials. Instead, these extreme values are used as numerical boundary conditions to probe the theoretical performance envelope of the device within the SCAPS framework and to identify qualitative trends that can guide future experimental trajectories [13]. Accordingly, performance values obtained at the highest doping levels should be interpreted strictly as upper-bound outcomes under idealized electrostatic control, rather than as realistic device predictions.

Carrier mobilities for electrons and holes are assumed to be constant, as SCAPS-1D does not compute mobility variations with doping, defect density, or electric field. This commonly adopted simplification enables isolation of the influence of individual parameters on device behavior, while neglecting mobility degradation mechanisms that may occur in real materials (e.g., defect scattering, ion migra-

tion, or field-dependent transport) [14].

Bulk defect states are introduced in the absorber layers to represent non-radiative recombination via an effective dominant defect level with a fixed energy position and identical electron/hole capture cross-sections. This approach does not aim to reproduce the full microscopic defect spectrum, but rather to capture effective recombination behavior suitable for comparative parametric analysis. Interface defect states between adjacent layers are also included at fixed densities; however, a dedicated sensitivity analysis of interfacial recombination is outside the scope of the present work and will be considered in future studies [15].

Table 1. Value of materials parameters.

Materials	CdS [9]	CdTe [3]	Perovskite [16]	Spiro-OMeTAD [17]
Eg (eV)	2.4	1.5	1.3	3.2
X (eV)	4.5	4.3	4.170	2.1
$\varepsilon/\varepsilon_0$	10	9.4	8.2	3
Nc (cm^{-3})	2.0×10^{18}	8×10^{17}	1×10^{18}	2.5×10^{18}
Nv (cm^{-3})	1.8×10^{19}	1.8×10^{19}	1×10^{19}	1.8×10^{19}
μe (cm^2/Vs)	100	320	2000	2×10^{-4}
μh (cm^2/Vs)	25	40	300	2×10^{-4}
Nd (cm^{-3})	1×10^{17}	1×10^{15}	-	-
Na (cm^{-3})	-	-	1×10^{15}	1×10^{17}
Ve (cm/s)	$1 \times 10^{+7}$	1×10^{7}	1×10^{7}	1×10^{7}
Vh (cm/s)	1×10^{7}	1×10^{7}	1×10^{7}	1×10^{7}
	Bulk defect			
Type of defect	Neutral	Acceptor	Donor	Neutral
Energy distribution	Single	Gaussian	Gaussian	Single
Concentration (cm^{-3})	$1 \times 10^{+15}$	$1 \times 10^{+15}$	$1 \times 10^{+15}$	$1 \times 10^{+15}$
	Interfacial defect			
Type of defect	Neutral			
Concentration (cm^{-2})	1×10^{10}			

In addition to the material parameters listed in Table 1, the global boundary conditions and numerical settings used in the SCAPS-1D simulations are summarized in Table 2. These parameters define the electrical contacts, illumination conditions, recombination mechanisms, and transport assumptions applied throughout the simulations.

Table 2. Simulation boundary conditions used in SCAPS-1D.

Parameter	Value	Description
Illumination spectrum	AM 1.5G	Standard solar spectrum
Light intensity	1000 $W \cdot m^{-2}$	Standard test condition
Operating temperature	300 K	Default SCAPS simulation temperature
Front contact material	ITO	Transparent conductive oxide
Front contact work function	4.7 eV	Ohmic contact with CdS
Back contact material	Ag	Metal electrode
Back contact work function	4.6 eV	Ohmic contact with Spiro-OMeTAD
Contact type	Ohmic	Ideal carrier extraction
Series resistance (Rs)	1×10^{-1} $\Omega \cdot cm^2$	Typical value used in thin-film solar cells
Shunt resistance (Rsh)	10^5 $\Omega \cdot cm^2$	Represents low leakage current
Optical absorption model	SCAPS analytical absorption model	Based on bandgap-dependent absorption coefficient
Carrier statistics	Maxwell-Boltzmann statistics	Default SCAPS assumption
Bandgap narrowing	Not included	Degeneracy effects neglected
Radiative recombination	Included	Band-to-band recombination
SRH recombination	Included	Dominant recombination mechanism
Auger recombination	Included	Relevant at high carrier density
Interface recombination velocity	10^7 $cm \cdot s^{-1}$	Typical SCAPS boundary value
Surface recombination velocity	10^7 $cm \cdot s^{-1}$	At front and back contacts

2.3. Settings Simulation

The solar-cell simulations were performed at a temperature of 300 K under standard AM 1.5G illumination with an incident power density of 100 $mW \cdot cm^{-2}$. These operating conditions correspond to standard photovoltaic testing protocols and enable direct comparison with previously reported experimental and numerical studies.

The series and shunt resistances were set to 1×10^{-1} $\Omega \cdot cm^2$ and 1×10^5 $\Omega \cdot cm^2$, respectively. These values were kept constant throughout the simulations in order to focus on the intrinsic influence of absorber and transport-layer properties on device performance. The selected resistances represent low-resistive and weak-leakage conditions and therefore minimize extrinsic losses associated with contact resistance and shunt pathways. Consequently, the reported device performances should be interpreted as reflecting intrinsic material and junction behavior rather than resistive-limit scenarios.

For the optical absorption of the active layers, the analytical model implemented

in SCAPS was adopted. The absorption coefficient is described by:

$$\alpha(h\nu) = A_0\sqrt{h\nu - E_g}$$

where A_0 is a constant (10^5 $cm^{-1}\cdot eV^{-1}$) and $h\nu$ represents the photon energy. This simplified expression corresponds to an idealized direct bandgap absorption behavior. It does not explicitly account for experimentally measured absorption spectra, Urbach tails, excitonic effects, or optical interference phenomena within the multilayer stack. The purpose of this approximation is to provide a controlled and consistent optical description suitable for comparative parametric analysis within the SCAPS framework [6] [15].

The optimization strategy consisted of varying one parameter at a time while keeping all others fixed. This one-parameter-at-a-time approach enables clear identification of the dominant physical influence of each parameter on the photovoltaic response. It should be emphasized that this methodology does not constitute a global multivariate optimization and does not explicitly capture possible interdependencies between parameters. The results are therefore intended to highlight sensitivity trends and theoretical performance envelopes rather than to define a unique globally optimized device configuration.

3. Results and Discussion

3.1. Influence of Layer Thickness of the p-Type $CH_3NH_3SnI_3$

The influence of the $CH_3NH_3SnI_3$ absorber thickness on the photovoltaic performance of the device is presented in **Figure 2(a)**. In this analysis, the doping concentration of $CH_3NH_3SnI_3$ was fixed at 1×10^{15} cm^{-3}. The CdTe layer thickness and doping concentration were maintained at 400 nm and 1×10^{15} cm^{-3}, respectively, while the CdS and Spiro-OMeTAD transport layers were kept at 30 nm with doping levels of 1×10^{17} cm^{-3}. This controlled configuration enables isolation of the sole effect of $CH_3NH_3SnI_3$ thickness on device behavior.

As the $CH_3NH_3SnI_3$ thickness increases from 100 nm to 1000 nm, the short-circuit current density (Jsc) increases from 27.680 $mA\cdot cm^{-2}$ to 34.744 $mA\cdot cm^{-2}$. This enhancement is attributed to improved photon absorption and increased photogeneration within the perovskite layer, consistent with drift-diffusion transport theory and previous numerical studies. A thicker absorber increases the optical path length, thereby enhancing carrier generation under AM 1.5G illumination [16].

Conversely, the open-circuit voltage (Voc) decreases from 1.020 V to 0.907 V as thickness increases. Within the drift-diffusion framework, Voc is governed by the balance between photogenerated current and recombination current. Increasing absorber thickness enlarges the volume in which bulk recombination can occur, which ultimately reduces Voc.

The fill factor (FF) exhibits a slight initial increase (from 75.30% to 76.52%), followed by a marginal decrease at higher thicknesses. The initial improvement is associated with enhanced photocurrent and moderate recombination, while the

subsequent decline reflects increased recombination losses that distort the J-V curve near Voc and reduce the squareness of the characteristic curve.

As a result, the power conversion efficiency (PCE) first increases from 21.25% to 24.17%, before slightly decreasing to 24.11% at larger thicknesses. This behavior reflects the competition between enhanced optical absorption and increased recombination losses. Similar thickness-dependent trends have been reported in previous simulation studies of perovskite-based and hybrid absorber solar cells [18].

These results highlight that, within the dual-absorber CdTe/$CH_3NH_3SnI_3$ configuration, an optimal perovskite thickness exists where photogeneration gains are balanced by manageable recombination losses, defining a practical theoretical thickness window under the present modeling assumptions.

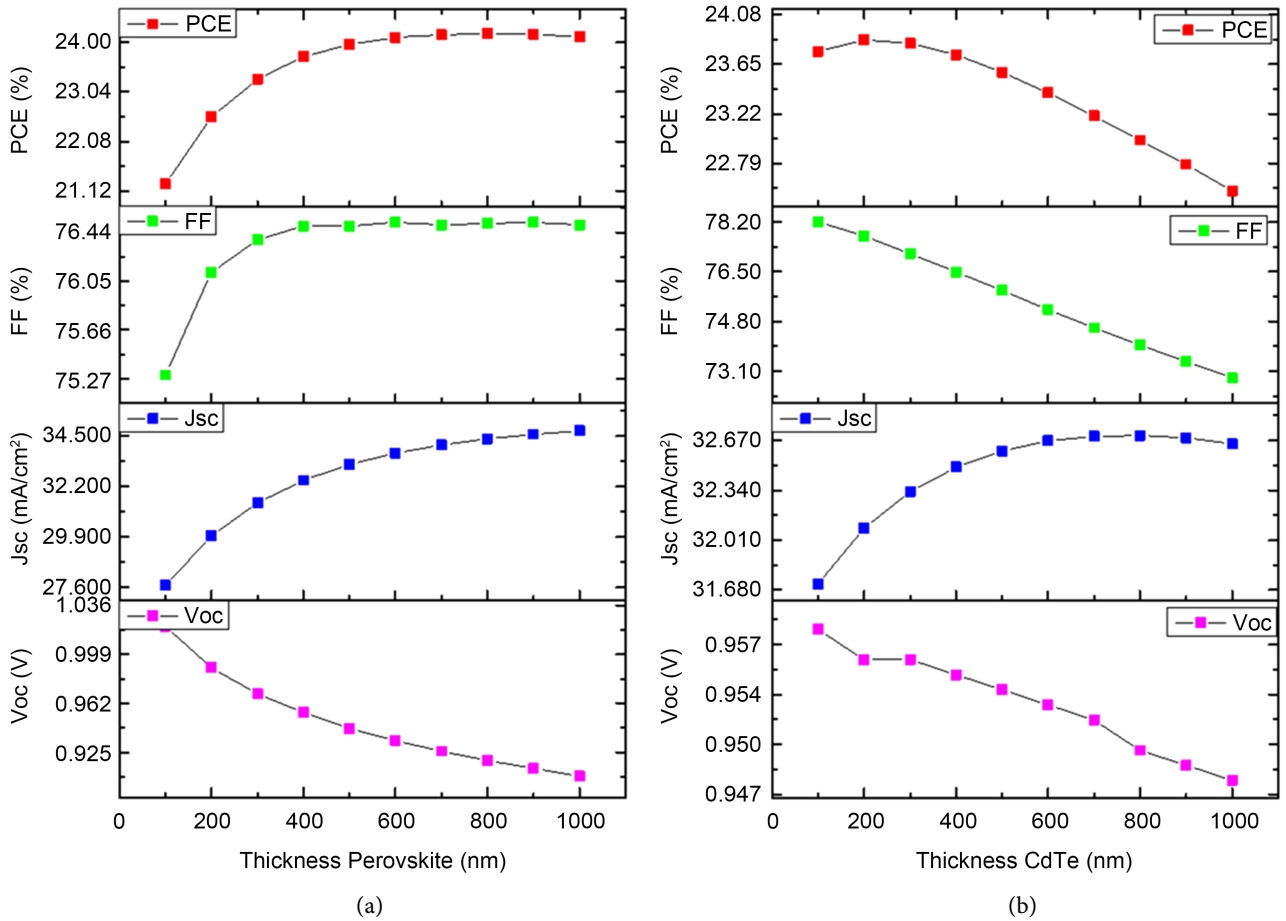

Figure 2. Influence of absorber layer thickness on photovoltaic parameters: (a) $CH_3NH_3SnI_3$ layer; (b) CdTe layer.

3.2. Influence of Layer Thickness of the n-Type CdTe

To isolate the effect of CdTe thickness, the $CH_3NH_3SnI_3$ layer was kept constant at 400 nm with a doping concentration of 1×10^{15} cm^{-3}. The CdS and Spiro-OMeTAD transport layers were maintained at 30 nm each, and all other parameters were fixed according to Table 1.

As shown in **Figure 2(b)**, increasing the CdTe thickness from 100 nm to 1000 nm initially enhances the short-circuit current density (Jsc), followed by a saturation behavior beyond approximately 500 nm. This trend is attributed to increased photon absorption within the CdTe layer at smaller thicknesses. Once the optical absorption becomes nearly complete, further thickness increase does not significantly enhance photogeneration, leading to current saturation [9].

The open-circuit voltage (Voc) exhibits only a modest variation, decreasing slightly from 0.958 V to 0.942 V across the investigated thickness range. In a dual-absorber heterojunction, Voc is governed by the overall recombination current and the quasi-Fermi level splitting across the full device stack rather than by absorber thickness alone. The relatively weak sensitivity of Voc to CdTe thickness indicates that bulk recombination within CdTe remains moderate under the present doping conditions, and that the dominant recombination pathways are not significantly altered within this thickness interval [19].

In contrast, the fill factor (FF) decreases from 78.21% to 70.40% as CdTe thickness increases. Since the series resistance is kept constant in the simulations, this reduction cannot be attributed to resistive effects. Instead, it is associated with enhanced bulk recombination in the thicker CdTe region, which modifies the slope of the J-V curve near the maximum power point and reduces the squareness of the characteristic curve [20].

As a consequence, the power conversion efficiency (PCE) first increases, reaching a maximum value of 23.86% around 400 nm, before decreasing to 21.34% at larger thicknesses. This behavior reflects the competition between improved photogeneration at moderate thickness and increased volume recombination at excessive thickness. These results suggest the existence of an optimal CdTe thickness window within the present modeling assumptions, beyond which recombination losses outweigh optical gains [21].

3.3. Influence of Perovskite Doping

The electrical behavior of the CdTe/$CH_3NH_3SnI_3$ heterojunction is strongly influenced by the acceptor doping concentration (N_A) in the perovskite absorber. As shown in **Figure 3(a)**, Voc, Jsc, FF, and PCE remain nearly constant when N_A varies between 1×10^{11} cm^{-3} and 1×10^{15} cm^{-3}, with typical values of 0.955 V for Voc, 32.473 $mA \cdot cm^{-2}$ for Jsc, 75.67% for FF, and 23.46% for PCE. In this low-doping regime, the depletion width extends significantly into the perovskite layer, and charge collection is primarily governed by optical generation and drift-assisted extraction rather than by doping-induced electric-field modulation.

For N_A values exceeding 1×10^{15} cm^{-3}, a marked increase in Voc, FF, and PCE is observed. Increasing p-type doping shifts the Fermi level closer to the valence band and modifies the electrostatic band bending at the CdTe/$CH_3NH_3SnI_3$ interface. The resulting enhancement of the built-in potential strengthens carrier separation and reduces recombination within the depletion region, leading to an increase in the quasi-Fermi level splitting and thus in Voc. However, as reported in

previous studies [22], the maximum achievable Voc is ultimately limited by non-radiative recombination processes. The observed saturation of Voc at high N_A values therefore indicates a transition toward a recombination-limited regime rather than indefinite enhancement of the internal electric field.

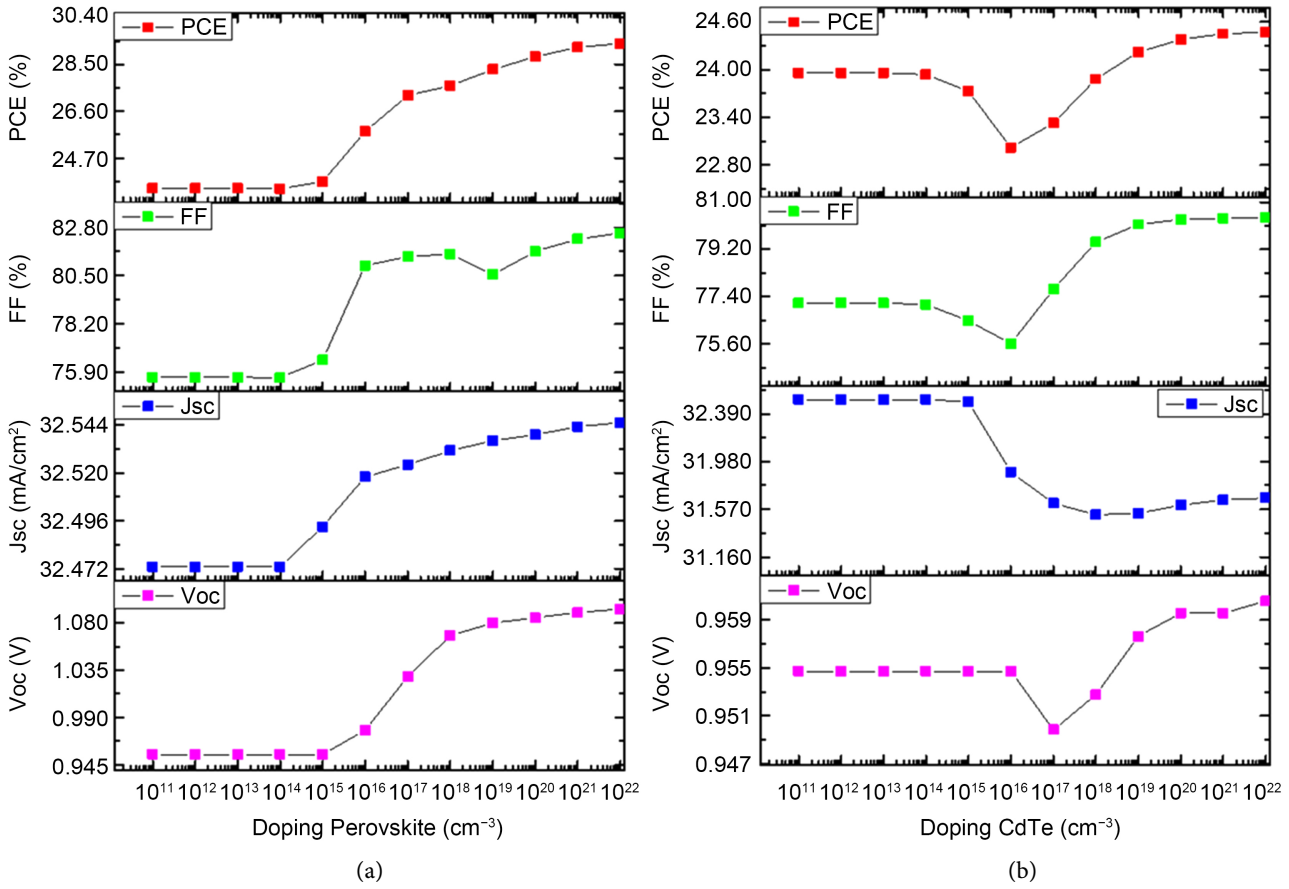

Figure 3. Influence of active layer doping: (a) $CH_3NH_3SnI_3$; (b) CdTe.

The short-circuit current density (Jsc) exhibits only minor variation in the low-doping range, as photogeneration remains primarily governed by optical absorption. At higher doping levels, a moderate increase in Jsc is observed. This behavior is attributed to improved carrier collection efficiency and reduced bulk recombination probability under stronger internal electric fields, rather than to changes in optical generation itself.

The fill factor (FF) increases progressively from 75.67% to 82.53% as N_A approaches 1×10^{22} cm^{-3}. Since the external series resistance is fixed in the simulations, this improvement reflects enhanced internal conductivity of the perovskite layer and reduced recombination-induced curvature in the J-V characteristics near the maximum power point.

The power conversion efficiency (PCE) follows the combined evolution of Voc and FF, increasing from approximately 23.46% to 29.36% as N_A varies from 1×10^{11} to 1×10^{22} cm^{-3}. It should be emphasized that the upper end of this doping

range represents highly idealized numerical boundary conditions within the SCAPS framework. Degeneracy effects, bandgap narrowing, Auger recombination, and mobility degradation at extreme doping levels are not explicitly included in the model. Therefore, the maximum efficiencies obtained at very high N_A values define a theoretical electrostatic performance envelope rather than experimentally realistic device behavior.

3.4. Influence of CdTe Layer Doping

In this analysis, the perovskite absorber was kept at a fixed acceptor doping concentration of 1×10^{15} cm^{-3}. The influence of the donor doping concentration (N_D) in CdTe on the photovoltaic parameters is presented in **Figure 3(b)**.

For N_D values up to approximately 1×10^{16} cm^{-3}, the photovoltaic parameters remain nearly unchanged. In this low-to-moderate doping regime, the depletion region extends substantially into the CdTe layer, and carrier collection is largely governed by drift-assisted transport within the space-charge region.

As N_D increases beyond this range, a distinct trend emerges: Voc and FF increase, while Jsc exhibits a slight decrease. The reduction in Jsc at higher N_D values can be attributed to the redistribution and narrowing of the depletion region on the CdTe side of the junction. As donor concentration increases, the space-charge region becomes progressively confined toward the lower-doped perovskite layer. Consequently, photogenerated carriers in CdTe are increasingly collected via diffusion rather than drift. If the minority-carrier diffusion length is comparable to or shorter than the quasi-neutral region thickness, bulk recombination increases, leading to a modest reduction in Jsc.

In contrast, increasing CdTe doping enhances band bending and strengthens the built-in electric field at the heterojunction. This stronger internal field improves carrier separation and reduces recombination in the depletion region, contributing to an increase in the quasi-Fermi level splitting and thus in Voc. The fill factor (FF) also improves due to enhanced junction electrostatics and reduced recombination-induced curvature in the J-V characteristic near the maximum power point. Since the external series resistance is fixed in the simulations, this FF improvement arises from internal electrostatic effects rather than resistive changes.

At higher N_D values, the combined enhancement in Voc and FF outweighs the moderate reduction in Jsc, leading to an overall increase in PCE. It should be emphasized, however, that very high donor concentrations represent idealized numerical conditions within the SCAPS framework. Effects such as bandgap narrowing, degeneracy, and Auger recombination at extreme doping levels are not explicitly included in the model. Therefore, the highest efficiencies obtained in this regime define a theoretical electrostatic limit rather than an experimentally validated device configuration.

3.5. Optimized Cell Parameter Values

Following the parametric analyses conducted at 300 K, an optimized device con-

figuration was constructed within the numerical framework described in Section 2.2. The objective of this optimization was not to determine a rigorously global optimum, but rather to identify a consistent high-performance configuration within the idealized modeling assumptions adopted in this study.

The optimized device results from the combined implementation of parameter values that exhibited favorable trends in the one-parameter-at-a-time analyses presented in Sections 3.1 - 3.4. Because electrostatic coupling and recombination processes in dual-absorber heterojunctions are inherently nonlinear, the resulting configuration should be interpreted as a numerically consistent near-optimal point rather than a mathematically exhaustive global solution.

The optimized structural and doping parameters are summarized in Table 3.

Table 3. Optimized values of thickness, doping and maximum defect of materials.

Layers	Thickness (μm)		N_A (cm^{-3})
CdS	0.030		1×10^{15}
CdTe	0.480		1×10^{17}
Perovskite ($CH_3NH_3SnI_3$)	0.400		1×10^{15}
Spiro-OMeTAD	0.030		1×10^{17}
Optimized photovoltaic parameters			
Voc (V)	**Jsc ($mA \cdot cm^{-2}$)**	**FF (%)**	**PCE (%)**
1.017	34.429	82.07	28.73

The optimized absorber thicknesses (0.400 μm for $CH_3NH_3SnI_3$ and 0.480 μm for CdTe) represent a compromise between enhanced optical absorption and recombination/transport limitations identified in previous sections. When both absorbers operate simultaneously, electrostatic coupling shifts the optimal thickness away from the values obtained in isolated thickness scans, highlighting the importance of considering the coupled system.

Using this optimized configuration, the simulated J-V characteristic under AM 1.5G illumination (100 $mW \cdot cm^{-2}$) at 300 K is shown in Figure 4.

The efficiency enhancement arises from the combined improvement in internal electric-field distribution, balanced absorber thicknesses, and reduced recombination under the adopted numerical assumptions.

It must be emphasized that this performance represents a theoretical upper-bound estimate obtained under idealized simulation conditions. The model does not include bandgap narrowing, degeneracy corrections, Auger recombination, mobility degradation at high doping, or realistic interface disorder beyond fixed defect densities. Consequently, the reported efficiency should be interpreted as defining the electrostatic and recombination-limited performance envelope of the architecture rather than as an experimentally validated device metric.

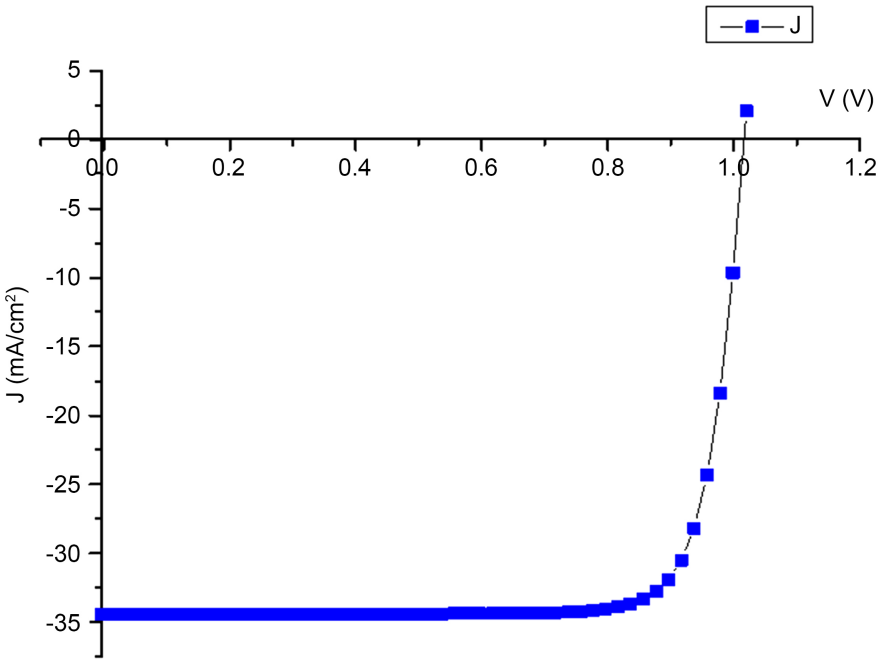

Figure 4. J(V) curve of the optimised solar cell.

3.6. Influence of Temperature on Solar Cell Parameters

The temperature dependence of the optimized device was investigated in the range 290 - 500 K using the structural and doping parameters defined in Section 3.5. Although this temperature range exceeds standard operating conditions, it enables evaluation of the intrinsic thermal sensitivity of the heterojunction within the limits of the adopted numerical framework.

As shown in **Figure 5**, increasing temperature leads to a systematic decrease in the open-circuit voltage (Voc), fill factor (FF), and overall power conversion efficiency (PCE), while the short-circuit current density (Jsc) exhibits a slight increase.

The moderate increase in Jsc with temperature is primarily attributed to bandgap narrowing in the absorber materials, which slightly extends the absorption edge and enhances photogeneration. However, this effect remains limited over the investigated range and does not compensate for the dominant recombination-related losses affecting the other parameters [23].

The temperature dependence of Voc can be understood from the diode relation:

$$\mathrm{Voc} \approx \frac{\mathrm{KT}}{\mathrm{q}} \ln\left(\frac{\mathrm{Jsc}}{\mathrm{J}_0} + 1\right)$$

where J_0 is the saturation current density. As temperature increases, J_0 rises significantly due to enhanced intrinsic carrier concentration and thermally activated recombination processes. This increase in J_0 reduces the quasi-Fermi level splitting and leads to a pronounced decline in Voc. The temperature-induced increase of the term kT/q further contributes to the reduction in voltage stability at elevated temperatures.

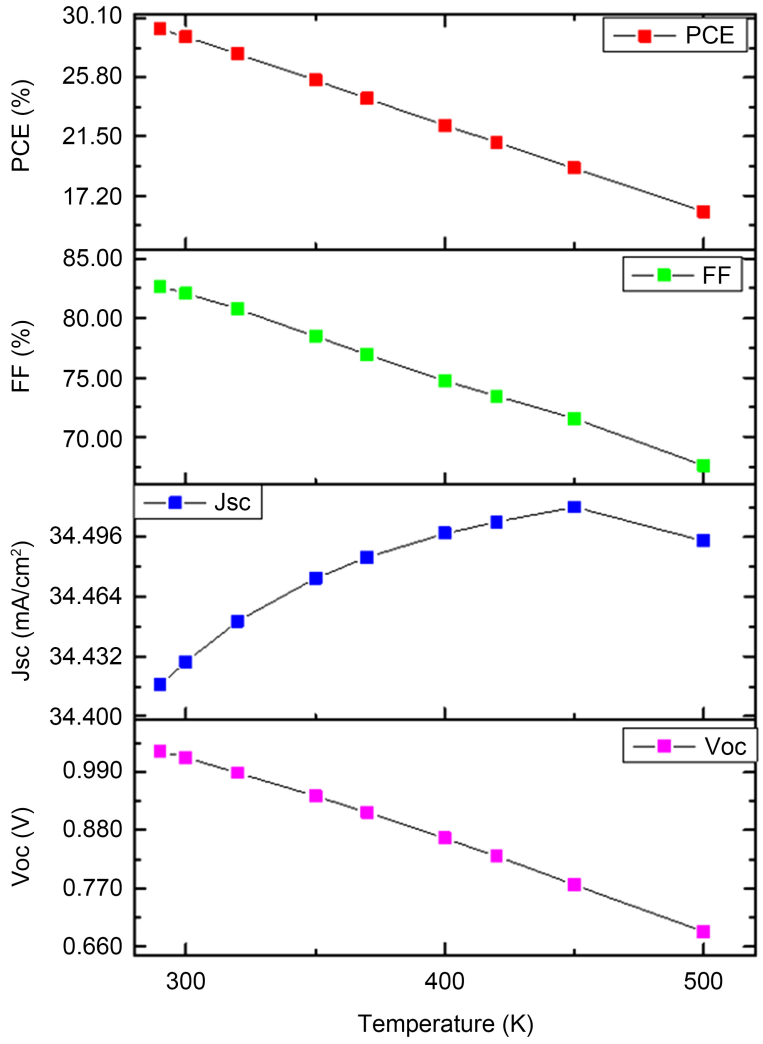

Figure 5. Influence of temperature on solar cell parameters.

The fill factor (FF) also decreases with temperature. Since the series and shunt resistances were kept constant in the simulations, the observed FF degradation arises primarily from intrinsic recombination effects and changes in diode ideality behavior rather than from resistive losses. The increased recombination modifies the slope of the J-V curve near the maximum power point, thereby reducing FF.

As a consequence of the simultaneous reduction in Voc and FF, the overall power conversion efficiency declines markedly with temperature. It should be emphasized that the present simulations do not include additional temperature-dependent mechanisms such as mobility degradation, ion migration, interface instability, or material phase transitions. Therefore, the reported trends reflect the intrinsic behavior predicted by the drift-diffusion model implemented in SCAPS and should be interpreted within these modeling limitations [13] [24].

3.7. Optimization Summary

The optimization procedure performed in this study enabled the identification of a

numerically consistent high-performance parameter set for the CdTe/$CH_3NH_3SnI_3$ dual-absorber heterojunction under the adopted modeling assumptions. The optimization focused primarily on absorber thicknesses and doping concentrations, while the transport-layer properties were kept constant in order to isolate the intrinsic electrostatic and recombination effects within the active junction.

For the CdTe absorber, thicknesses in the range of approximately 400 - 500 nm provided a favorable balance between optical absorption and recombination losses. Within this window, additional thickness increases did not significantly enhance Jsc due to absorption saturation, while recombination losses began to dominate. The selected optimized value therefore represents a compromise between optical gain and electrical transport constraints [25].

For the $CH_3NH_3SnI_3$ absorber, a thickness of 400 nm was identified as providing sufficient light harvesting while maintaining effective electric-field distribution across the heterojunction. When both absorbers operate simultaneously, the electrostatic coupling between layers shifts the optimal thickness away from the values obtained in isolated scans, emphasizing the importance of considering the full coupled system rather than independent layers [26].

Regarding doping, moderate p-type doping in the perovskite layer and controlled n-type doping in CdTe were found to produce the most favorable electrostatic configuration. Increasing the acceptor concentration in the perovskite enhances the built-in potential and strengthens the junction electric field, thereby improving carrier separation and Voc up to a recombination-limited regime. Conversely, excessively high donor doping in CdTe narrows the depletion region on the n-side and may increase recombination in quasi-neutral regions. The optimized configuration thus reflects a balance between field enhancement and recombination control rather than a simple monotonic dependence on doping magnitude [2].

The resulting J-V characteristics reveal that the dual-absorber configuration allows simultaneous enhancement of voltage and current contributions under idealized conditions, owing to complementary absorption and redistributed electric-field profiles within the coupled structure. However, the term "optimization" here should be understood within the constraints of the one-parameter-at-a-time methodology and the simplified physical model implemented in SCAPS.

Overall, the trends identified in this work highlight the importance of jointly engineering absorber thickness, doping, and defect densities in dual-absorber heterojunction architectures. These findings provide modeling-based design insights that may guide future experimental exploration, while recognizing that additional physical mechanisms—such as interface chemistry, contact resistivity, mobility degradation, and temperature-dependent effects—must be addressed for realistic device implementation.

To ensure the physical consistency of the simulated device performance, it is useful to compare the obtained efficiencies with the well-known Shockley-Queisser detailed-balance limit for single-junction solar cells. The Shockley-Queisser limit

predicts a maximum efficiency of approximately 29% - 30% for an ideal single absorber with a bandgap near 1.34 eV under AM1.5G illumination. In the present configuration, the device consists of a single-terminal dual-absorber heterojunction composed of CdTe (Eg ≈ 1.5 eV) and $CH_3NH_3SnI_3$ (Eg ≈ 1.3 eV). Within the SCAPS drift-diffusion framework, the two absorbers contribute jointly to the overall photogeneration while remaining electrically coupled through a single p-n junction [27].

Under idealized assumptions, such as perfectly selective contacts, negligible series resistance, low defect densities, and efficient carrier collection, the combined absorption of the two layers can increase the simulated photocurrent while maintaining a high open-circuit voltage determined by the electrostatic properties of the heterojunction. Consequently, simulated efficiencies slightly above the classical single-absorber Shockley-Queisser limit may appear in numerical studies of multi-absorber single-terminal architectures. However, it should be emphasized that such values represent theoretical upper limits within the adopted modeling assumptions and should not be interpreted as experimentally achievable device efficiencies. The purpose of the present analysis is therefore to identify physically consistent design trends and electrostatic regimes rather than to predict record experimental performance.

3.8. Comparative Study

To ensure methodological consistency, the comparative analysis was restricted to SCAPS-based numerical studies employing $CH_3NH_3SnI_3$ as the primary absorber. This approach allows meaningful comparison within a similar drift-diffusion simulation framework, reducing discrepancies arising from fundamentally different modeling methodologies.

Table 4 summarizes key photovoltaic parameters reported in representative peer-reviewed SCAPS studies of $CH_3NH_3SnI_3$-based solar cells. Most previously reported devices rely on single-absorber architectures such as FTO/TiO_2/$CH_3NH_3SnI_3$/Spiro-OMeTAD/Au or ZnO/$CH_3NH_3SnI_3$/Cu_2O/Pt. Reported simulated efficiencies span a wide range (≈5% - 28%), reflecting variations in assumed defect densities, transport-layer properties, contact engineering, and doping conditions.

Earlier numerical investigations typically reported moderate efficiencies, often limited by non-radiative recombination and imperfect band alignment. Subsequent improvements were achieved through optimized transport layers, refined interface defect modeling, and enhanced electrostatic control, progressively increasing simulated performance.

Within this curated benchmark set, the CdTe/$CH_3NH_3SnI_3$ heterojunction developed in this work yields a simulated efficiency of 28.73% under the optimized and idealized conditions described in Sections 2 - 3. This value places the proposed architecture among the highest-performing SCAPS-based $CH_3NH_3SnI_3$ simulations reported to date [28].

Table 4. Comparison of performance among simulated PSCs based on $CH_3NH_3SnI_3$ with different device structures.

Ref.	Structure (simulation)	Voc (V)	Jsc ($mA \cdot cm^{-2}$)	FF (%)	PCE (%)	Journal
Du *et al.*, 2016	FTO/TiO_2/$CH_3NH_3SnI_3$/Spiro-OMeTAD/Au	0.89	35.32	77.45	24.36	*Chinese Phys. B*
Shamna *et al.*, 2020	FTO/NiO/$CH_3NH_3SnI_3$/PCBM/Al	0.98	33.45	70.33	22.95	*Mater. Today Proc.*
Salem *et al.*, 2021	FTO/TiO_2/$CH_3NH_3SnI_3$/Spiro-OMeTAD/Au	0.67	17.60	44.20	5.15	*Energies*
Patel, 2021	FTO/TiO_2/$CH_3NH_3SnI_3$/Cu_2O/Pt	0.93	40.14	75.78	28.39	*Sci. Rep.*
Qasim *et al.*, 2022	ITO/ZnO/CdTe/$CH_3NH_3SnI_3$/CuSCN/Au	0.82	34.05	76.57	21.24	*Solar Energy*
Omarova *et al.*, 2022	TiO_2/$CH_3NH_3SnI_3$/Cu_2O/Pt	1.02	32.60	84.05	27.95	*$Crystals*
Imani *et al.*, 2023	TCO/TiO_2/$CH_3NH_3SnI_3$/Cu-HTL/Au	0.97	34.34	85.17	28.32	*Appl. Phys. A*
This work	CdS/CdTe/$CH_3NH_3SnI_3$/Spiro-OMeTAD	**1.017**	34.429	82.07	28.73	

It is important to emphasize that numerical efficiencies reported in the literature, including the present work, are strongly dependent on modeling assumptions such as defect densities, carrier mobilities, interface properties, and contact ideality. Direct comparison must therefore be interpreted within the limits of each study's adopted parameters.

The enhanced performance observed in the dual-absorber configuration can be attributed to complementary optical absorption and modified electric-field distribution across the coupled heterojunction. The slightly smaller bandgap of $CH_3NH_3SnI_3$ extends absorption toward longer wavelengths, while CdTe contributes strong absorption in the visible range. The presence of two absorbers redistributes the internal electric field and influences carrier separation dynamics at the CdTe/$CH_3NH_3SnI_3$ interface. Optimized transport layers further facilitate selective carrier extraction and reduce back-injection losses within the adopted model [29].

This comparison does not aim to claim absolute superiority over previously reported designs, but rather to illustrate how dual-absorber architectures can shift the theoretical performance envelope within SCAPS-based numerical studies of lead-free perovskite systems. The present results highlight the potential of coupled absorber engineering as a design strategy, while recognizing that experimental validation and more comprehensive physical modeling remain essential for realistic device assessment.

3.9. Limitations of the Study

The numerical results presented in this work were obtained using the SCAPS-1D simulation framework, which relies on a one-dimensional, steady-state drift-diffusion description of charge transport and recombination in multilayer photovoltaic devices. While SCAPS is widely established for thin-film solar-cell modeling, its formulation inherently involves simplifying assumptions that define the bound-

aries of the present analysis [12].

First, the simulations assume spatially uniform material properties within each layer and a strictly one-dimensional geometry. Effects such as lateral inhomogeneities, grain-boundary transport, current crowding, and local compositional fluctuations are not included. Consequently, the simulated device represents an idealized planar structure rather than a microstructurally complex thin film [26].

Second, the optimization strategy employed in Sections 2.1 - 2.4 varied absorber thickness and doping concentration independently to isolate individual physical trends. In practical devices, these parameters are often interdependent. For instance, increasing the acceptor concentration in $CH_3NH_3SnI_3$ may influence defect formation energy, carrier mobility, and interface quality simultaneously effects that are not explicitly coupled within the present drift-diffusion framework [26].

Third, the CdTe/$CH_3NH_3SnI_3$ interface was treated as an abrupt heterojunction with fixed electronic properties. Real interfaces may exhibit chemical interdiffusion, local band bending variations, non-uniform defect distributions, and interface dipoles. Such phenomena can significantly alter recombination dynamics and band alignment under experimental conditions [2].

Furthermore, the transport model does not explicitly account for bandgap narrowing at high doping levels, carrier degeneracy effects, Auger recombination, field-dependent mobility, or detailed temperature dependence of carrier mobility. These mechanisms may become relevant under the extreme doping or elevated temperature regimes explored in this work. As a result, the high photovoltaic efficiencies obtained under optimized conditions should be interpreted as defining an upper theoretical performance envelope within the adopted modeling assumptions rather than as directly predictive experimental values.

The temperature-dependent analysis presented in Section 2.6 addresses steady-state intrinsic behavior only. Long-term degradation mechanisms particularly relevant for tin-based perovskites such as Sn^{2+} oxidation, ion migration, phase instability, and moisture-induced degradation are not included in the model. Device stability therefore remains an open experimental question [30].

Despite these limitations, the relative trends identified in this study namely the influence of absorber thickness, doping level, and defect density on electrostatic distribution and recombination behavior are expected to remain qualitatively valid within broader physical contexts. While absolute efficiency values depend strongly on idealized assumptions, the modeling results provide physically motivated design insights for future experimental investigation of CdTe/perovskite dual-absorber heterojunctions.

4. Conclusions

In this work, a CdTe/$CH_3NH_3SnI_3$ dual-absorber heterojunction solar cell was systematically investigated using the SCAPS-1D drift-diffusion simulation framework. By combining a well-established thin-film absorber (CdTe) with a lead-free

tin-based perovskite, the proposed architecture was designed to explore the potential advantages of complementary optical absorption and redistributed electrostatic profiles within a coupled heterojunction structure.

A comprehensive parametric study was conducted to examine the influence of absorber thickness, doping concentration, defect density, and operating temperature on device performance. The results demonstrate that device behavior is strongly governed by the balance between electric-field distribution, recombination dynamics, and optical absorption in the two absorbers. In particular, the CdTe/$CH_3NH_3SnI_3$ interface plays a central role in determining voltage generation and carrier extraction efficiency [11] [12].

Under optimized and idealized numerical conditions, the proposed configuration reaches a simulated power conversion efficiency of 28.73%, with a high open-circuit voltage and a favorable fill factor. However, this value should be interpreted as defining a theoretical upper-performance envelope within the assumptions of the SCAPS model. The present study does not incorporate effects such as bandgap narrowing, carrier degeneracy, Auger recombination, detailed interface chemistry, or long-term degradation phenomena. Consequently, the absolute efficiency should not be regarded as directly predictive of experimentally achievable performance.

The primary contribution of this work lies in the identification of physically consistent parameter regimes and the clarification of how absorber thickness, doping levels, and defect densities collectively shape the electrostatic and recombination landscape of a dual-absorber heterojunction. The temperature-dependent analysis further highlights the intrinsic thermal sensitivity of the device, emphasizing the importance of recombination control and interface engineering.

Rather than claiming absolute performance superiority, this study provides a physics-driven exploration of the CdTe/$CH_3NH_3SnI_3$ architecture within a controlled numerical framework. The trends identified here offer modeling-based design insights that may guide future experimental investigations, particularly in the areas of junction engineering, controlled doping strategies, and interface defect management.

Future research should focus on experimental validation of the proposed architecture, advanced interface passivation strategies, and comprehensive stability assessment under operational conditions. Such efforts will be essential to determine the realistic performance limits and technological viability of CdTe/$CH_3NH_3SnI_3$-based dual-absorber solar cells.

Acknowledgements

The authors sincerely thank Dr. Marc Burgelmann and his team at the University of Gent, Belgium, for providing the scientific community with this simulation program. The authors gratefully acknowledge University of Man (U-Man), Department of Physics (Chemistry), Faculty of Science and Technology, for providing technical support and access to research and computational facilities used in

this work. They also acknowledge University of Nangui Abrogoua (UNA), Department of Mathematics, Physics and Informatics, for its scientific environment and academic support. In addition, the authors express their appreciation to Université Félix Houphouët-Boigny, Laboratory of Technologies (Lab-Tech), for their valuable institutional support and contribution to the successful completion of this study.

Conflicts of Interest

The authors declare no conflicts of interest regarding the publication of this paper.

References

[1] Jeyakumar, B., Vasudevan, T., Ramalingam, S. and Chen, L. (2025) Enhancing Perovskite Solar Cell Efficiency and Stability with P-(Trifluoromethyl and Trifluoromethoxy) Phenylboronic Acid Additives. *ACS Applied Energy Materials*, **8**, 11925-11935. https://doi.org/10.1021/acsaem.5c01079

[2] Rühle, S. (2016) Tabulated Values of the Shockley-Queisser Limit for Single Junction Solar Cells. *Solar Energy*, **130**, 139-147. https://doi.org/10.1016/j.solener.2016.02.015

[3] McCandless, B.E. and Sites, J.R. (2010) Cadmium Telluride Solar Cells. In: Luque, A. and Hegedus, S., Eds., *Handbook of Photovoltaic Science and Engineering*, Wiley, 600-641.

[4] Green, M.A., Dunlop, E.D., Yoshita, M., Kopidakis, N., Bothe, K., Siefer, G., *et al.* (2025) Solar Cell Efficiency Tables (Version 66). *Progress in Photovoltaics: Research and Applications*, **33**, 795-810. https://doi.org/10.1002/pip.3919

[5] Stranks, S.D. and Snaith, H.J. (2015) Metal-Halide Perovskites for Photovoltaic and Light-Emitting Devices. *Nature Nanotechnology*, **10**, 391-402. https://doi.org/10.1038/nnano.2015.90

[6] Noel, N.K., Stranks, S.D., Abate, A., Wehrenfennig, C., Guarnera, S., Haghighirad, A., *et al.* (2014) Lead-Free Organic-Inorganic Tin Halide Perovskites for Photovoltaic Applications. *Energy & Environmental Science*, **7**, 3061-3068. https://doi.org/10.1039/c4ee01076k

[7] Green, M.A., Ho-Baillie, A. and Snaith, H.J. (2014) The Emergence of Perovskite Solar Cells. *Nature Photonics*, **8**, 506-514. https://doi.org/10.1038/nphoton.2014.134

[8] Polman, A., Knight, M., Garnett, E.C., Ehrler, B. and Sinke, W.C. (2016) Photovoltaic Materials: Present Efficiencies and Future Challenges. *Science*, **352**, aad4424. https://doi.org/10.1126/science.aad4424

[9] Bhari, B.Z., Rahman, K.S., Chelvanathan, P. and Ibrahim, M.A. (2023) Numerical Simulation of Ultrathin CDTE Solar Cell by SCAPS-1D. *IOP Conference Series: Materials Science and Engineering*, **1278**, Article ID: 012002. https://doi.org/10.1088/1757-899x/1278/1/012002

[10] Biswas, B.C., Shimul, A.I., Ghosh, A., Awaad, N.S. and Ibrahium, H.A. (2025) Exploring Lead-free ca_3bicl_3-based Perovskite Solar Cells: A Computational Comparison of Charge Transport Layers with DFT and SCAPS-1D. *Journal of Computational Chemistry*, **46**, e70231. https://doi.org/10.1002/jcc.70231

[11] Decock, K., Khelifi, S. and Burgelman, M. (2011) Modelling Multivalent Defects in Thin Film Solar Cells. *Thin Solid Films*, **519**, 7481-7484. https://doi.org/10.1016/j.tsf.2010.12.039

[12] Burgelman, M., Nollet, P. and Degrave, S. (2000) Modelling Polycrystalline Semicon-

ductor Solar Cells. *Thin Solid Films*, **361**, 527-532. https://doi.org/10.1016/s0040-6090(99)00825-1

[13] Banik, S., Das, A., Das, B.K. and Islam, N. (2024) Numerical Simulation and Performance Optimization of a Lead-Free Inorganic Perovskite Solar Cell Using SCAPS-1D. *Heliyon*, **10**, e23985. https://doi.org/10.1016/j.heliyon.2024.e23985

[14] Biswas, B.C., Shimul, A.I., Alshihri, A.A., El-Rayyes, A., Khan, M.T. and Rahman, M.A. (2025) Design and Optimization of Ca_3BiI_3-Based Solar Cells through a Comprehensive Analysis of Optoelectronic Properties and Charge Transport Layers Using Simulation and ML. *Physica B: Condensed Matter*, **717**, Article ID: 417770. https://doi.org/10.1016/j.physb.2025.417770

[15] Sze, S.M. and Ng, K.K. (2007) Physics of Semiconductor Devices. Wiley. https://doi.org/10.1002/0470068329

[16] Patel, P.K. (2021) Device Simulation of Highly Efficient Eco-Friendly $CH_3NH_3SnI_3$ Perovskite Solar Cell. *Scientific Reports*, **11**, Article No. 3082. https://doi.org/10.1038/s41598-021-82817-w

[17] Minemoto, T. and Murata, M. (2014) Device Modeling of Perovskite Solar Cells Based on Structural Similarity with Thin Film Inorganic Semiconductor Solar Cells. *Journal of Applied Physics*, **116**, Article ID: 054505. https://doi.org/10.1063/1.4891982

[18] Ouslimane, T., Et-taya, L., Elmaimouni, L. and Benami, A. (2021) Impact of Absorber Layer Thickness, Defect Density, and Operating Temperature on the Performance of $MAPbI_3$ Solar Cells Based on ZnO Electron Transporting Material. *Heliyon*, **7**, e06379. https://doi.org/10.1016/j.heliyon.2021.e06379

[19] Mostafa, S.M.G., Utsho, K.I.F., Rahman, M.S., Tarekuzzaman, M., Alsalmi, O., Rasheduzzaman, M., *et al.* (2025) Device Engineering and Performance Analysis of $Cs_2AgSbBr_6$ Perovskite Solar Cells Using SCAPS-1D. *Inorganic Chemistry Communications*, **178**, Article ID: 114636. https://doi.org/10.1016/j.inoche.2025.114636

[20] Nelson, J. (2003) The Physics of Solar Cells. Imperial College Press. https://doi.org/10.1142/p276

[21] Parathraju, P. and Umasankar, P. (2025) Performance Evaluation of Ultrathin CdTe-Based Solar Cells with Dual Absorbers via SCAPS-1D Simulation. *Scientific Reports*, **15**, Article No. 26428. https://doi.org/10.1038/s41598-025-12006-6

[22] Stolterfoht, M., Wolff, C.M., Márquez, J.A., Zhang, S., Hages, C.J., Rothhardt, D., *et al.* (2018) Visualization and Suppression of Interfacial Recombination for High-Efficiency Large-Area Pin Perovskite Solar Cells. *Nature Energy*, **3**, 847-854. https://doi.org/10.1038/s41560-018-0219-8

[23] Skoplaki, E. and Palyvos, J.A. (2009) On the Temperature Dependence of Photovoltaic Module Electrical Performance: A Review of Efficiency/Power Correlations. *Solar Energy*, **83**, 614-624. https://doi.org/10.1016/j.solener.2008.10.008

[24] Shafi, M.A., Ullah, H., Ullah, S., Khan, L., Bibi, S. and Soucase, B.M. (2022) Numerical Simulation of Lead-Free Sn-Based Perovskite Solar Cell by Using SCAPS-1D. *Engineering Proceedings*, **12**, Article 92. https://doi.org/10.3390/engproc2021012092

[25] Minemoto, T. and Murata, M. (2014) Impact of Work Function of Back Contact of Perovskite Solar Cells without Hole Transport Material Analyzed by Device Simulation. *Current Applied Physics*, **14**, 1428-1433. https://doi.org/10.1016/j.cap.2014.08.002

[26] Kirchartz, T. and Rau, U. (2018) What Makes a Good Solar Cell? *Advanced Energy Materials*, **8**, Article ID: 1703385. https://doi.org/10.1002/aenm.201703385

[27] Sultana, B., Rahman, M.M., Harun-Or-Rashid, M., Haque, M.D., Irfan, A., Chaudhry, A.R., *et al.* (2024) A New Design and Optimization of SnSe-Based Dual Absorber Solar Cell with Efficiency above 28%. *Journal of Nanoparticle Research*, **26**, Article No. 181. https://doi.org/10.1007/s11051-024-06085-1

[28] Shimul, A.I., Biswas, B.C., Keya, L.R., Islam, S., Rahman, M.A., KRIAA, K., *et al.* (2026) Machine Learning Guided Optimization of Lead Free $K_2TlSbCl_6$/Na_2ScAuI_6 Dual Absorber Double Perovskite Solar Cells. *Solar Energy*, **307**, Article ID: 114348. https://doi.org/10.1016/j.solener.2026.114348

[29] Chandra Biswas, B., Kriaa, K., Shimul, A.I., Maatki, C., Rahman, M.A. and Elboughdir, N. (2025) Deep Insights into Lead-Free Sr_3BiI_3-Based Anti-Perovskite Solar Cells: Optimization Strategies and Impedance Spectroscopy *via* Numerical Simulation and Machine Learning. *RSC Advances*, **15**, 43702-43726. https://doi.org/10.1039/d5ra07289a

[30] Hao, F., Stoumpos, C.C., Cao, D.H., Chang, R.P.H. and Kanatzidis, M.G. (2014) Lead-free Solid-State Organic-Inorganic Halide Perovskite Solar Cells. *Nature Photonics*, **8**, 489-494. https://doi.org/10.1038/nphoton.2014.82